A FAST INTEGRATED MOBILITY SPECTROMETER FOR RAPID MEASUREMENT OF SUB-MICROMETER AEROSOL SIZE DISTRIBUTION, PART II: EXPERIMENTAL CHARACTERIZATION

Wang, J., Pikridas, M., Pinterich, T., Spielman, S. R., Tsang, T.,
McMahon, A., and Smith, S.

May 2017

Environmental & Climate Science Dept.

Brookhaven National Laboratory

U.S. Department of Energy
DOE Office of Science

DISCLAIMER

A fast integrated mobility spectrometer for rapid measurement of sub-micrometer aerosol size distribution, Part II: Experimental characterization

Jian Wang[1*], Michael Pikridas[1†], Tamara Pinterich[1], Steven R. Spielman[2], Thomas Tsang[3], Andrew McMahon[1], Scott Smith[1]

[1]Environmental and Climate Sciences Department, Brookhaven National Laboratory, Upton, New York 11973, USA

[2]Aerosol Dynamics Inc., Berkeley, California 94710, USA

[3]Instrumentation Division, Brookhaven National Laboratory, Upton, New York 11973, USA

Abstract

A Fast Integrated Mobility Spectrometer (FIMS) with a wide dynamic size range has been developed for rapid aerosol size distribution measurements. The design and model evaluation of the FIMS are presented in the preceding paper (Paper I), and this paper focuses on the experimental characterization of the FIMS. Monodisperse aerosol with diameter ranging from 8 to 600 nm was generated using Differential Mobility Analyzer (DMA), and was measured by the FIMS in parallel with a Condensation Particle Counter (CPC). The mean particle diameter measured by the FIMS is in good agreement with the DMA centroid diameter. Comparison of the particle concentrations measured by the FIMS and CPC indicates the FIMS detection efficiency is essentially 100% for particles with diameters of 8 nm or larger. For particles smaller than 20 nm or larger than 200 nm, FIMS transfer function and resolution can be well represented by the calculated ones based on simulated particle trajectories in the FIMS. For particles between 20 and 200 nm, the FIMS transfer function is boarder than the calculated, likely due to non-ideality of the electric field, including edge effects near the end of the electrode, which are not represented by the 2-D electric field used to simulate particle trajectories.

Keywords: Fast Integrated Mobility Spectrometer; Aerosol size distribution; High time resolution; Electrical mobility; Transfer function; Mobility resolution.

---

[*] Author to whom correspondence should be addressed: jian@bnl.gov
[†] Current affiliation: The Cyprus Institute, Environment Energy and Water Research Center, Nicosia, Cyprus

1 Introduction

A Fast Integrated Mobility Spectrometer (FIMS) with a particle diameter range of 8 to 600 nm has been developed for rapid measurement of aerosol size distribution. The design and model evaluation of the FIMS are presented in the preceding paper (Paper I). By employing a spatially varying electric field (J. Wang, 2009), the FIMS provides a significant improvement in dynamic size range compared to the previous version (Kulkarni & Wang, 2006a, 2006b; Olfert, Kulkarni, & Wang, 2008; Olfert & Wang, 2009). Inside the separator of the new FIMS, charged particles are first separated by the spatially varying electric field into different flow streamlines based on their electrical mobility. The electric field creates regions with drastically different field strengths, such that particles of a wide size range can be simultaneously classified and subsequently measured. After grown into super-micrometer droplets in a condenser, the spatially separated droplets are imaged by a high speed CCD camera. The images provide mobility-dependent particle positions and counts, which are used to derive particle electrical mobility and concentration. As particles of a wide size range are detected simultaneously, the FIMS provides significant increases in both measurement speed and counting statistics compared to traditional scanning mobility techniques (e.g., Scanning Mobility Particle Sizer, S. C. Wang & Flagan, 1990). This paper describes the design and performance characterization of this new FIMS with an improved dynamic size range.

The characterization of the new FIMS followed the same approach used to evaluate the performance of the previous version (Kulkarni & Wang, 2006b), and is briefly reviewed below. Cylindrical DMAs (Model 3081 and 3085, TSI Inc.) were used to generate monodisperse calibration aerosols, which were then measured by the FIMS in parallel with a condensation particle counter (CPC). The diameter of the monodisperse aerosol measured by the FIMS is compared to the DMA centroid diameter to characterize the FIMS sizing accuracy, and the FIMS detection efficiency is derived from the concentrations measured by the FIMS and the CPC as a function of particle diameter. The FIMS transfer function and mobility resolutions are studied by examining the responses of the FIMS to the monodisperse aerosols classified by the DMA. The FIMS responses to DMA classified particles are calculated using the FIMS transfer function simulated in Paper I, and are compared with the measurements. The reasons for the discrepancies

55   between the measured and calculated FIMS responses, and the implications on the FIMS
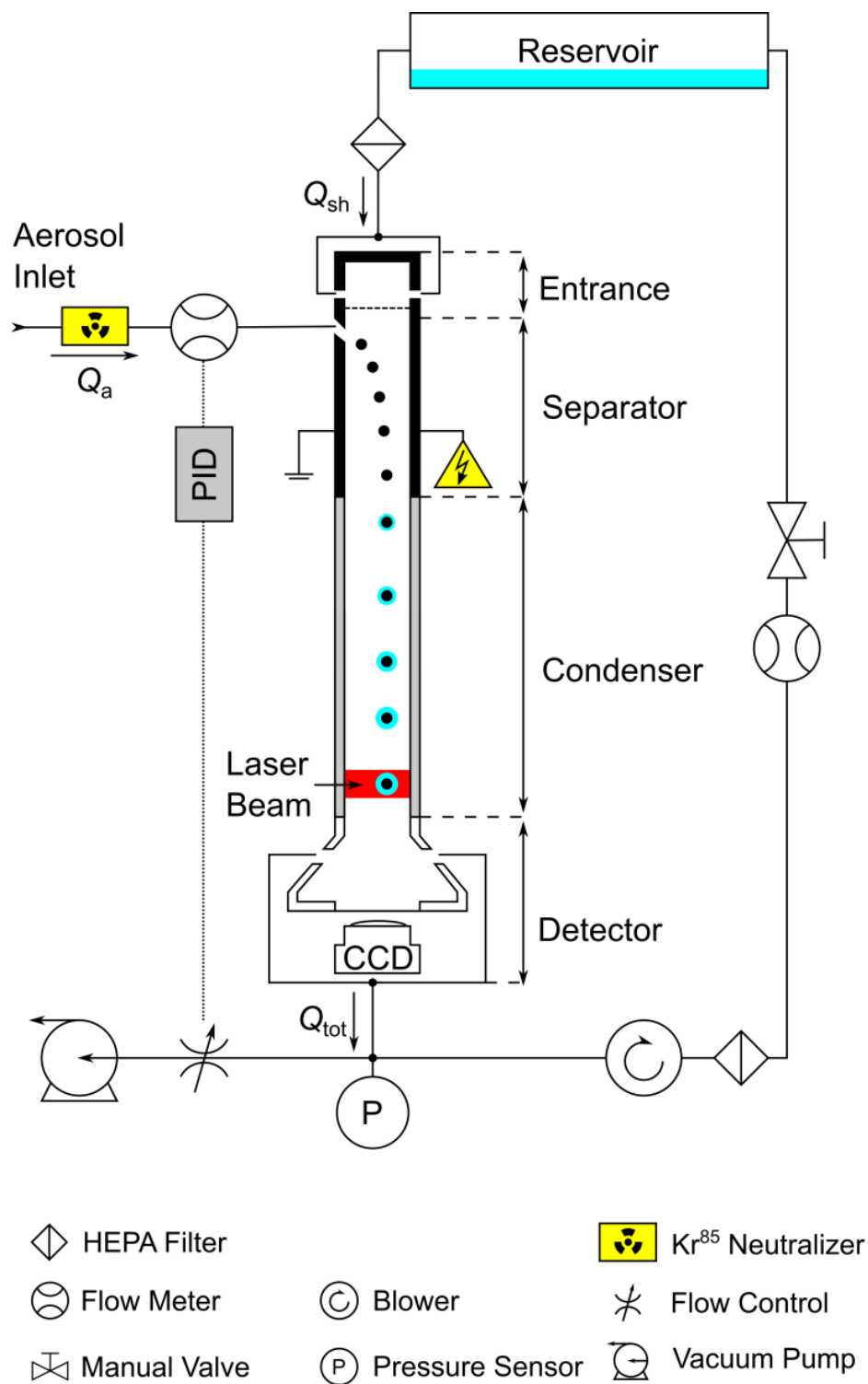   mobility resolutions are examined and discussed.

Figure 1. Schematic of the FIMS with improved dynamic size range.

2 Instrument design and experimental setup

2.1 Instrument design

The design of the FIMS with improved dynamic size range closely resembles that of the original FIMS employing a uniform electric field (Kulkarni & Wang, 2006a). The key differences include the electrode inside the separator and the minor modifications of the physical dimensions as described in Paper I. The physical dimensions and operation conditions are present in Table 1 of Paper I. A schematic of the FIMS is shown in Fig. 1. The FIMS has three major sections - (i) separator, (ii) condenser, and (iii) detector, which are arranged sequentially to form a rectangular channel with a clear cross-sectional area of 1.12×12.7 cm. At the exit of the condenser, grown particles are illuminated by a sheet of laser light and imaged by a CCD camera. The counts and positions of particles within an area of 0.672×7.0 cm (i.e., 0.224 cm $\leq x$ $\leq$ 0.896 cm, -3.5 cm $\leq y \leq$ 3.5 cm, as described in Paper I) in the center of the cross section are retrieved from the recorded images, and are used to derive particle sizes and concentrations. As in Paper I, the coordinate system depicted in Fig. 1 of J. Wang (2009) is used here to describe particle and grown droplet positions.

The sheath flow and the vast majority of the exhaust flow of the FIMS are operated in a closed recirculation loop. The sheath flow is supplied by a blower controlled by a PID module at the desired flow rate (Q_{sh}) of 13 L min^{-1}, which is monitored by a flowmeter (Alicat Scientific Inc.). The aerosol flow rate (Q_a) of the FIMS is monitored by measuring the pressure drop across a laminar flow element, located just upstream of the aerosol inlet. Additional exhaust flow is controlled by a vacuum pump along with a proportional solenoid valve to maintain the desired aerosol flow of 0.26 L min^{-1}. Prior to entering the FIMS, the particle-free sheath flow is saturated with heptanol vapor in a reservoir. The walls of the condenser are cooled to 20°C below the temperature of reservoir using thermoelectric coolers controlled by a PID module, and the condenser temperature is monitored using thermistors mounted on the outer walls of the condenser. For the experiments reported here the temperatures of the reservoir and condenser were 23 and 3°C, respectively. The images recorded by the CCD camera are 8-bit grayscale. For derivation of particle positions, each image is first converted to a binary image by applying an intensity threshold that clearly differentiates the particle images from the background. The center

of the converted particle binary image is then computed and taken as the particle position in the cross section (i.e., *x-y* plane).
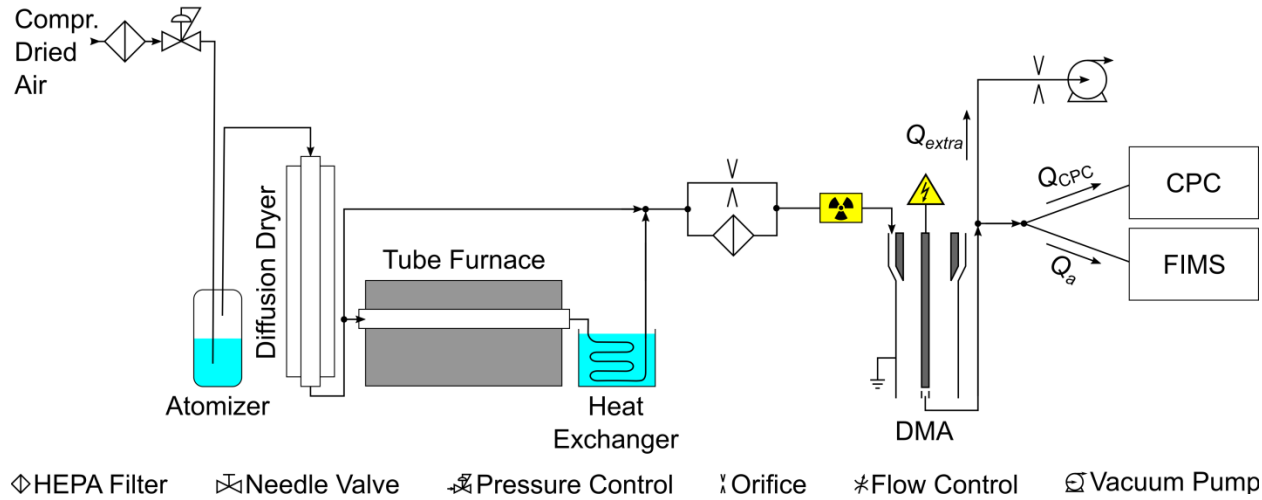

Figure 2. Experimental setup used to characterize the performance of the FIMS.

2.2 Experimental Setup

The Experimental setup used to characterize FIMS is shown in Fig. 2. Ammonium sulfate aerosols were generated by atomizing $(NH_4)_2SO_4$ solutions, and subsequently dried in a diffusion dryer. The direct output from the Atomizer provided particles ranging from 50 to 650 nm for the experiments. The atomized particles were also evaporated in a tube furnace and recondensed to produce a polydispersed aerosol ranging from 5 to 50 nm. The polydispersed aerosols generated by either of the two methods were subsequently diluted and classified by either a DMA (TSI Inc. Model 3081) or a Nano-DMA (TSI Inc., model 3085) to produce monodisperse aerosol with diameter ranging from 8 nm to 600 nm. The classified, monodisperse aerosol was then split and directed to the FIMS and a condensation particle counter (CPC; TSI Inc, Model 3025A) operated in parallel, except for classified particles with diameter larger than 500 nm, for which all monodispersed aerosol flow was sent to the FIMS. The aerosol neutralizer of the FIMS was removed during these experiments to avoid any potential uncertainty introduced by particle charging efficiency (i.e., all classified particles introduced into the FIMS remained charged). For experiments at some of the particle diameters, the DMA monodispersed flow rate was higher than the sum of FIMS and CPC flow rates, and a critical orifice was used to remove the extra

5

flow of 0.56 L min^{-1}. The minimum (V_1) and maximum voltage (V_2) applied to the first and last
traces of the FIMS electrode were set at 20 and 8000 V, respectively. The DMA type and its
corresponding flow rates, which were optimized to achieve good DMA size resolution, are listed
in Table 1 for each classified particle diameter. All FIMS and upstream DMA flows were
calibrated with a flow calibrator (Gilibrator, Gilian Instruments); and the variability of the flows
was estimated to be less than 2%. All the data and image acquisition was carried out using
LabVIEW (National Instruments).

Table 1. The type of DMA, its corresponding flow rates, and rate of extra flow (Q_{extra}) used
during experiments for each of classified particle diameters. The DMA flow rates include those
of aerosol (Q_a), sheath (Q_{sh}), excess (Q_{ex}), and monodispersed (Q_m) flows.

D_p (nm)	DMA type	Q_a (L min^{-1})	Q_{sh} (L min^{-1})	Q_{ex} (L min^{-1})	Q_m (L min^{-1})	Q_{extra} (L min^{-1})
8	Nano DMA	1.12	11.3	11.3	1.12	0.56
9	Nano DMA	1.12	11.3	11.3	1.12	0.56
10	Nano DMA	1.12	11.3	11.3	1.12	0.56
12	Nano DMA	1.12	11.3	11.3	1.12	0.56
15	Nano DMA	1.12	11.3	11.3	1.12	0.56
20	Nano DMA	1.12	11.3	11.3	1.12	0.56
40	Nano DMA	1.12	11.3	11.3	1.12	0.56
60	Nano DMA	1.12	11.3	11.3	1.12	0.56
80	DMA	1.12	11.3	11.3	1.12	0.56
100	DMA	1.12	11.3	11.3	1.12	0.56
150	DMA	1.12	11.3	11.3	1.12	0.56
200	DMA	0.56	5.67	5.67	0.56	N/A
300	DMA	0.56	5.67	5.67	0.56	N/A
400	DMA	0.56	5.67	5.67	0.56	N/A
450	DMA	0.56	5.67	5.67	0.56	N/A
500	DMA	0.26	2.77	2.77	0.26	N/A
600	DMA	0.26	2.77	2.77	0.26	N/A
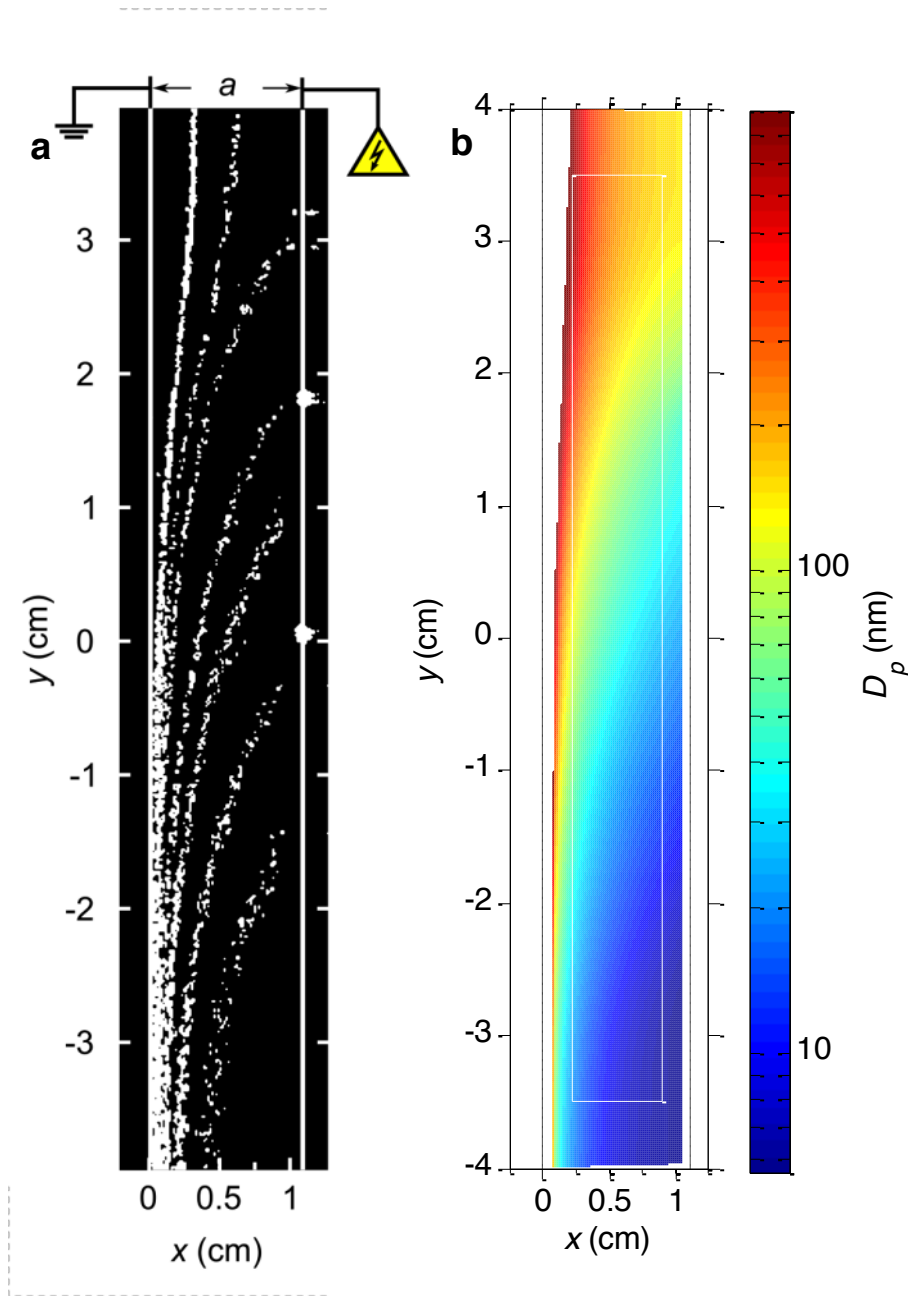
Figure 3. (a) Superimposed droplet images recorded during the measurements of DMA classified particles with diameters of 10, 20, 40, 60, 100, 200 and 400 nm. The two vertical solid lines represent the walls of the channel. (b) Detected positions of non-diffusing particles introduced along central aerosol flow streamline, simulated with V_1 and V_2 of 20 and 8000 V, respectively. The particle position is colored by particle diameter, and the two vertical dashed lines represent the walls of the condenser. The area within white rectangle represents the viewing window.

3 Results and Discussion

3.1 Size measurement with DMA classified aerosol

The first step in processing the recorded images is to calculate particle positions, in both x and y-coordinates, and total particle counts in each image. Figure 3 show the examples of measured positions of DMA classified particles with diameters ranging from 10 to 400 nm, and simulated positions of non-diffusing particles introduced along the central aerosol inlet flow streamline. As expected, large particles of low electrical mobility are spatially separated in the upper region of the channel cross section where the electric field is stronger, while in the lower region they remain close to the ground electrode where they were initially introduced. In the upper region, small particles of high electrical mobility travel too fast, and they either are lost on the HV electrode or exit the separator outside the viewing window. Small particles are instead classified in the lower region where the field is weaker.

The positions of grown particles are then converted to the FIMS response mobility Z_p^* by interpolation using the simulated Z_p^* map as a function of detected particle x-y position (e.g., Fig. 4b of paper I). The mobility distribution of the monodisperse aerosol classified by the DMA, combined with the width of FIMS transfer function leads to a distribution of the detected particle position, and therefore Z_p^*. An example of normalized Z_p^* distribution measured by the FIMS for DMA classified 40 nm particles is shown in Fig. 6. For the comparison of FIMS measured and DMA classified diameters, the instrument response mobility Z_p^* is also converted to instrument response diameter D_p^* assuming singly charged particles.

As described in paper I, the electric field is created by a PCB electrode consisting of 61 straight copper traces. The minimum (V_1) and maximum (V_2) voltages, supplied by HV voltage modules, are applied to the first and last traces. Voltages for the rest 59 traces are generated by a network of resistor dividers. Effective minimum and maximum voltages are derived in an effort to account for some of the instrument non-ideality, including the edge effects of electric field that are not represented by the 2-D electric field. The effective voltages are then used to simulate the 2-D electric field, particle trajectories, and the map of Z_p^* for the evaluations of the FIMS performance. This is very similar to the approach employed for the original FIMS. The

difference is that for the original FIMS operating with a single separating voltage, an effective

155 electrode length instead of effective HV was used to account for the instrument non-ideality, including the edge effect of the electric field. The effective V_1 and V_2 were derived using the following approach. The electrophoretic migration of large particles near the top of viewing window is strongly influenced by the maximum HV (V_2). An effective V_2 (8250 V) is therefore derived as the voltage that leads to the best agreement between the diameter classified by the

160 DMA and the average diameter measured by the FIMS (i.e., average D_p^*) for particles detected near the top of the viewing window (i.e., 2.0 cm $\leq y \leq$ 3.5 cm, 0.224 cm $\leq x \leq$ 0.896 cm). Similarly, an effective V_1 of 14.8 V yields the best agreement between the classified and the average measured diameters for particles detected near the bottom of the viewing window (i.e., -3.5 cm $\leq y \leq$ -2.0 cm, 0.224 cm $\leq x \leq$ 0.896 cm).
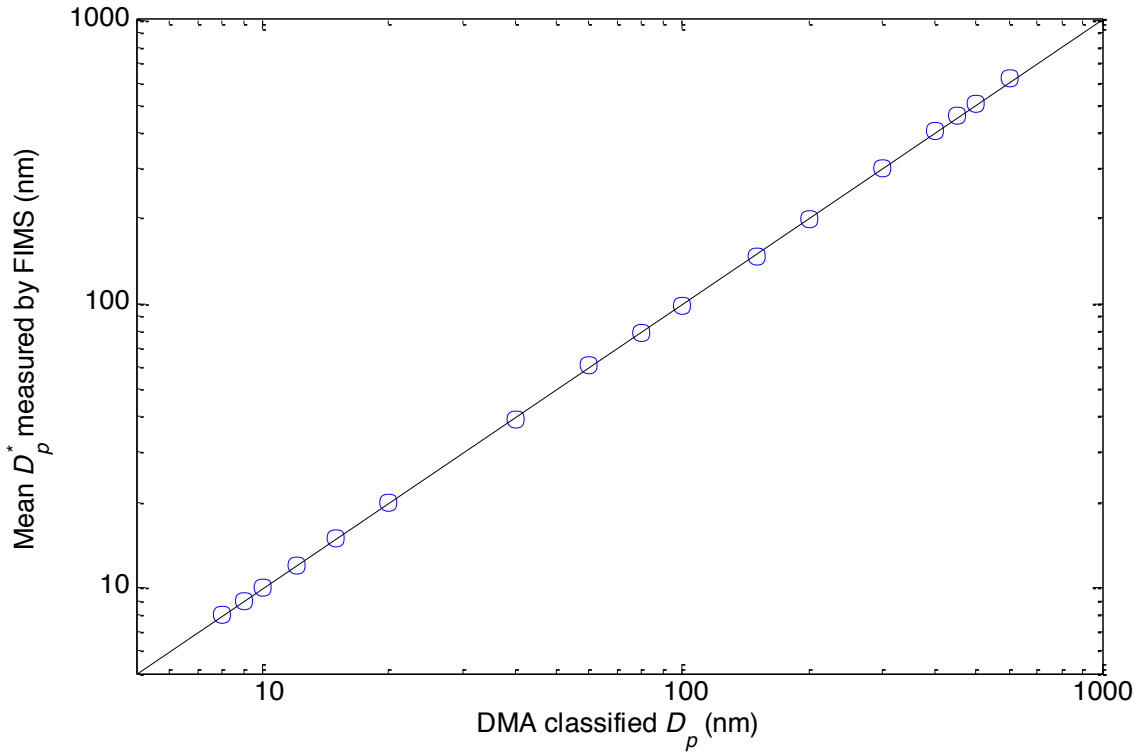
165

Figure 4. Comparison of the mean diameter (D_p^*) measured by the FIMS with DMA classified particle diameter.

9

The particle trajectories are then simulated using the effective V_1 and V_2 to create the map

170   of Z_p^* in the channel cross section. The x-y position of DMA classified particles retrieved from

the images is converted to Z_p^* using the map, which is then converted to D_p^*. The mean D_p^*

measured by the FIMS agrees well with the DMA centroid diameter calculated from the DMA

flow rates and classifying voltage over the entire size range studied (i.e., 8 to 600 nm, Fig. 4).

The maximum deviation of the mean measured D_p^* from the DMA centroid diameter is 3% at

175   600 nm. This result indicates that particle diameter can be measured by the FIMS with high

accuracy using the calibrated effective V_1 and V_2.

3.2 Counting and detection efficiencies of the FIMS

The overall counting efficiency of the FIMS is derived from the concentration of particles

180   (N_{FIMS}) detected within the viewing window and that simultaneously measured by the CPC

(N_{CPC}) for each of DMA classified particle diameters:

$$\eta = \frac{\eta_{CPC} \cdot N_{FIMS}}{N_{CPC}}, \tag{1}$$

where η_{CPC} represents the detection efficiency of the CPC 3025, which is essentially 100% for

the size range studied here. N_{FIMS} is given by:

185    $$N_{FIMS} = \frac{n_{\Delta t}}{\Delta t \cdot Q_a}, \tag{2}$$

where $n_{\Delta t}$ is the total number of particles detected within the viewing window during the

measurement period Δt, and Q_a is the FIMS aerosol sample flow rate (i.e., 0.26 L min^{-1}). The

counting efficiency η of FIMS is the product of three factors:

$$\eta = \eta_{pen} \cdot \eta_{trans} \cdot \eta_{det}, \tag{3}$$

10

190   where η_{pen}, η_{trans} and η_{det} are penetration, transmission and detection efficiencies, respectively. Here η_{pen} describes the fraction of particles that survive the transport in the FIMS inlet line, i.e. the flow passage between instrument inlet and separator, which consists of a series of tubing and narrow rectangular flow channels, including the aerosol inlet slit in the grounded electrode. The penetration efficiency through the tubing leading to the separator was characterized

195   experimentally at the aerosol flow rate of 0.26 L min^{-1}. The penetration efficiency through the slit entrance and the narrow gap upstream of it (see Fig. 1 of Kulkarni & Wang, 2006b) is calculated using Eq. (10) from Lee and Gieseke (1980).

    The transmission efficiency η_{trans} describes the fraction of particles entering the separator through the slit entrance that exit the FIMS condenser (i.e., where they are illuminated by the

200   laser light) within the viewing window, and is determined numerically based on simulated particle trajectories described earlier. This size dependent transmission efficiency η_{trans} is shown in Fig. 7a of paper I for particle diameter ranging from 8 to 700 nm. The detection efficiency η_{det}, representing the fraction of the particles within the viewing window that are successfully detected by the camera, is given by

205    $$\eta_{det} = \frac{N_{WFIMS}}{N_{CPC}} \cdot \frac{\eta_{CPC}}{\eta_{pen} \cdot \eta_{trans}} \qquad\qquad (4)$$

η_{det} depends on whether particles are activated and grow to sufficient sizes to be detected optically, which is controlled by particle diameter and the local saturation ratio along the particle trajectories in the condenser. Figure 5 shows that η_{det} is essentially 100% over the entire particle diameter range of 8 to 600 nm examined in this study. The minor deviation from unity, all within

210   10%, is likely to due to the uncertainties of both FIMS and CPC measurements. The essentially 100% detection efficiency is consistent with the simulation results in Paper I that particles as small as 8 nm are activated and grow into super-micrometer droplets within the viewing window. This also suggests that calculated penetration and transmission efficiencies capture particle losses and transport sufficiently well.
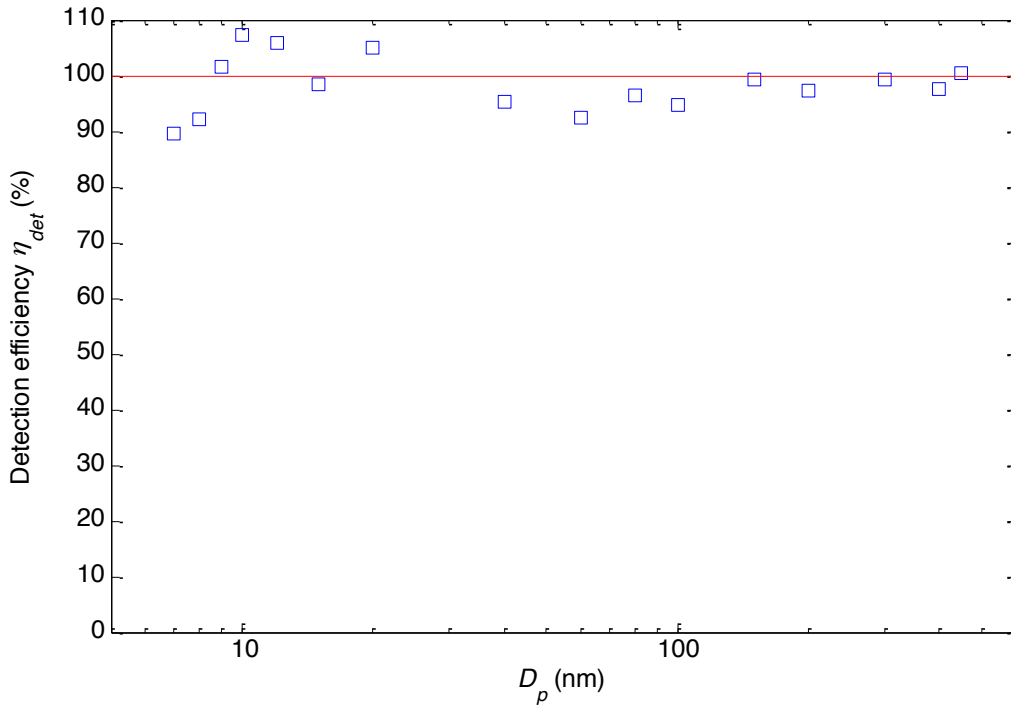
215

Figure 5. Detection efficiency of the FIMS as a function of particle diameter.

3.3 Transfer function and mobility resolutions

As discussed in Paper I, Brownian diffusion can substantially broaden the FIMS transfer function and decrease the FIMS mobility resolutions of small particles. As an analytic form of the transfer function is not available for the FIMS employing the spatially varying electric field, it is very challenging to characterize FIMS transfer function experimentally through fitting a few controlling parameters as was done in Kulkarni and Wang (2006b). Here we examine the FIMS transfer function by comparing the calculated and measured responses of the FIMS to monodisperse particles classified by a DMA. Let $n_1(Z_p)$ represent the mobility distribution of the polydisperse aerosol introduced into the DMA, the distribution of the monodisperse aerosol classified by the DMA is then given by $n_1(Z_p)\,\Omega(Z^*_{p,DMA}, Z_p)$, where $\Omega(Z^*_{p,DMA}, Z_p)$ is the DMA transfer function and $Z^*_{p,DMA}$ the centroid mobility corresponding to the DMA classifying voltage and flow rates. Particle charging efficiency and penetration efficiencies within both the DMA

12

230   and the plumbing system have been omitted in the above formula and are represented by an effective distribution $n_1(Z_p)$. The response of the FIMS to the DMA classified aerosol, described by the Z_p^* distribution measured by the FIMS, is:

$$\left(\frac{dN}{dZ_p^*}\right)_{FIMS} = \int_0^{\infty} n_1(Z_p) \, \Omega(Z_{p,DMA}^*, Z_p) \, P(Z_p, Z_p^*) \, dZ_p. \tag{5}$$

The DMA transfer function $\Omega(Z_{p,DMA}^*, Z_p)$ is evaluated using the formula given by Stolzenburg

235   (1988), and $P(Z_p, Z_p^*)$ is derived from particle trajectories simulated using effective V_1 and V_2 as described in Paper I. Given the widths of both $\Omega(Z_{p,DMA}^*, Z_p)$ and $P(Z_p, Z_p^*)$, the product of $\Omega(Z_{p,DMA}^*, Z_p)$ and $P(Z_p, Z_p^*)$ has non-negligible value only within a very narrow range of Z_p near $Z_{p,DMA}^*$, if any at all. As a result, $n_1(Z_p)$ can be treated as a constant within this narrow Z_p range for the integration in Eq. (5), and a normalized Z_p^* distribution $\frac{dN}{dZ_p^*}$, defined as $\frac{dN}{dZ_p^*}$

240   divided by its maximum value, can be calculated using $\Omega(Z_{p,DMA}^*, Z_p)$ and simulated $P(Z_p, Z_p^*)$. The normalized $\frac{dN}{dZ_p^*}$ are calculated from $P(Z_p, Z_p^*)$ based on simulated trajectories assuming L_a values of 5.9 and 13.5 cm, respectively, and are compared with the measured distributions. Here L_a represents the distance traveled by a particle between the end of the electrode and the point of activation in the condenser as described in Paper I. An example for 40 nm particles classified by

245   the DMA is shown in Fig. 6. There are very minor differences between the calculated $\frac{dN}{dZ_p^*}$ based on simulations assuming the two different L_a values. The measured $\frac{dN}{dZ_p^*}$ is generally in agreement with the calculated, but exhibits a somewhat broader distribution, which is further examined below.
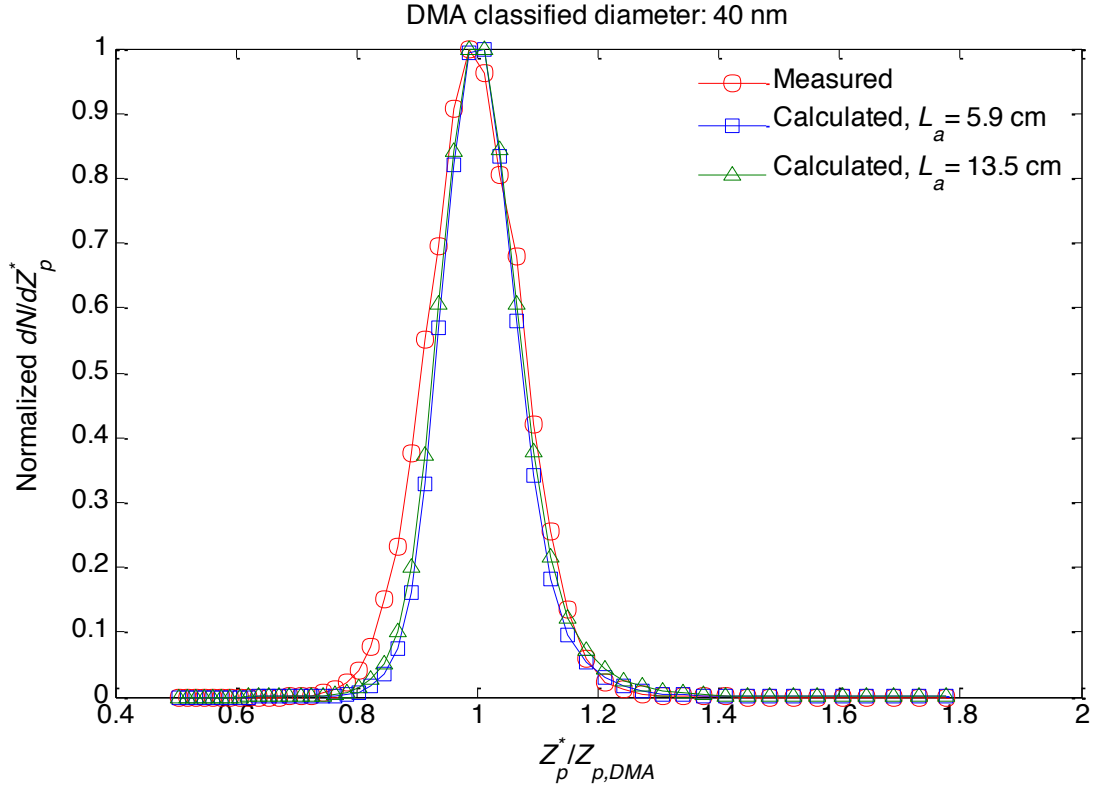
250 Figure 6. Normalized Z_p^* distribution $\dfrac{\sum_i dN}{dZ_p^*}$ measured by the FIMS and calculated using Eq. (5)
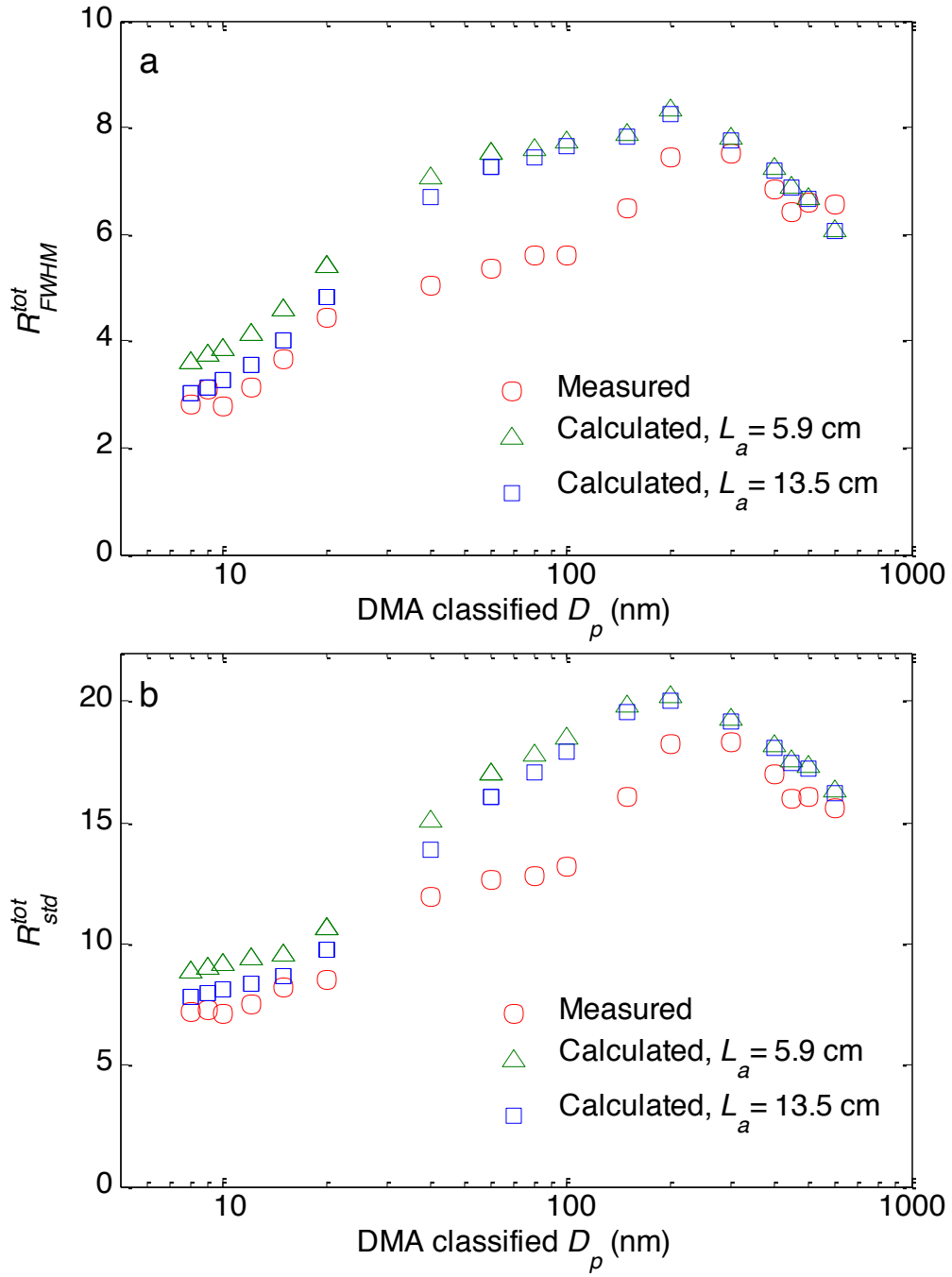
for 40 nm DMA classified particles.

Figure 7. (a) R_{FWHM}^{tot} and (b) R_{std}^{tot} derived from measured $\dfrac{dN}{dZ_p^*}$ and those calculated from FIMS

255   transfer functions based on two different L_a values.

To compare the measured and simulated FIMS response to DMA classified particles, we introduce an overall mobility resolution of the DMA-FIMS system, R_{FWHM}^{tot} as

$$R_{FWHM}^{tot}\left(Z_{p,DMA}\right) = \overline{Z_p^*} \Big/ \Delta Z_p^* \qquad (6)$$

where $\overline{Z_p^*}$ and ΔZ_p^* are the mean Z_p^* value and the full width at half maximum of the

260 distribution $\dfrac{dN}{dZ_p^*}$, respectively. Similarly, an overall resolution R_{std}^{tot} is defined as:

$$R_{std}^{tot}\left(Z_{p,DMA}\right) = \overline{Z_p^*} \Big/ \sigma_{Z_p^*} \qquad (7)$$

where $\sigma_{Z_p^*}$ is the standard deviation in Z_p^* derived from the distribution $\dfrac{dN}{dZ_p^*}$. The values of ΔZ_p^*

and $\sigma_{Z_p^*}$, which reflect the spread of the $\dfrac{dN}{dZ_p^*}$, are due to the combination of the widths of both

DMA and FIMS transfer functions as shown in Eq. (5). Figure 7 shows the R_{FWHM}^{tot} and R_{std}^{tot}

265 derived from the measured distribution $\dfrac{dN}{dZ_p^*}$, and those calculated using simulated FIMS

transfer functions. There are relatively minor differences between calculated total resolutions based on the two different L_a values. This is consistent with the small impact of the choice of L_a value on the resolution of simulated FIMS transfer function (paper 1). The differences between measured and calculated total resolutions are quite minor for particles smaller than 20 nm or

270 larger than 200 nm in diameter, suggesting that the FIMS transfer function and mobility resolutions are well represented by the calculations. However, the measured total resolutions for particles with diameters between 20 and 200 nm are substantially lower than those calculated based on simulated FIMS transfer functions.
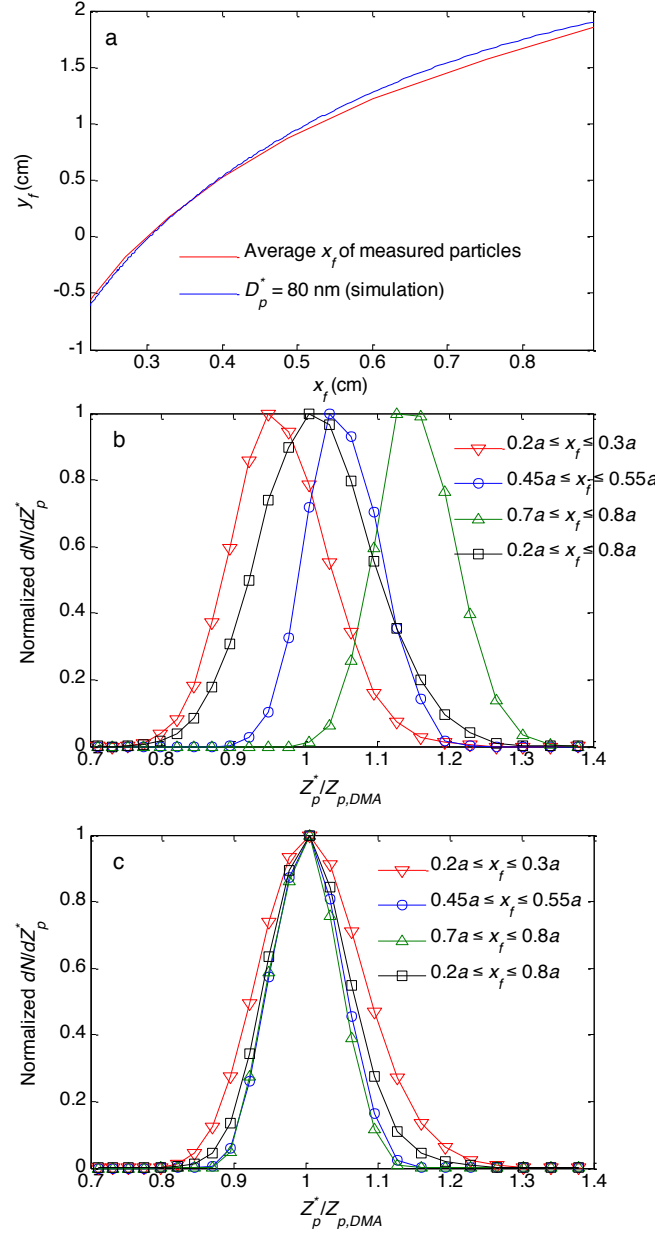
275

Figure 8. (a) The average x_f position of DMA classified 80 nm particles measured by the FIMS as a function of y_f, and simulated particle x_f-y_f positions corresponding to D_p^* of 80 nm, (b) measured distribution $\frac{\sum dN}{dZ_p^*}$ for particles detected within different ranges of x_f position, and (c) simulated distribution $\frac{\sum dN}{dZ_p^*}$ based on L_a of 13.5 cm for particles detected within different ranges of x_f position.

The cause of the discrepancy between measured and calculated resolutions is illustrated in Fig. 8. Let x_f and y_f denote particle x and y positions detected at the exit of the condenser. Figure 8a shows the average x_f as a function of y_f for DMA classified 80 nm particles. For particles detected towards the right side of the viewing window (i.e., near the HV electrode), the average x_f is on the right side of the line corresponding to D_p^* of 80 nm, suggesting on average, these particles are measured by the FIMS with diameters less than 80 nm (i.e., higher mobility). In contrast, for particles detected near the ground electrode, the average x_f is on the left side of the line corresponding to D_p^* of 80 nm, indicating that the average measured D_p^* is larger than 80 nm (i.e., lower mobility). This shift of measured D_p^* and therefore Z_p^* is further illustrated in Fig. 8b, which shows the measured distribution $\frac{dN}{dZ_p^*}$ for particles detected within different ranges of x_f. The measured $\frac{dN}{dZ_p^*}$ shifts toward larger Z_p^* as x_f increases. In contrast, the simulated $\frac{dN}{dZ_p^*}$ is centered at $Z_{p,DMA}^*$, regardless of the range of x_f. While the measured overall $\frac{dN}{dZ_p^*}$ for particle detected within the entire viewing window is centered around $Z_{p,DMA}^*$, the shift of $\frac{dN}{dZ_p^*}$ in Z_p^* space with x_f leads to a broadening of the overall $\frac{dN}{dZ_p^*}$, therefore lower R_{FWHM}^{tot} and R_{std}^{tot} values. It is worth noting that R_{FWHM}^{tot} and R_{std}^{tot} values are substantially lower than the calculated values for classified particles with diameters between 20 and 200 nm, and particles within this size range are detected over the entire range of x_f (i.e., from $0.2a$ to $0.8a$) within the viewing window (Fig. 3b). In comparison, particles smaller than 20 nm or greater than 200 nm are detected with narrower x_f ranges within the viewing window.
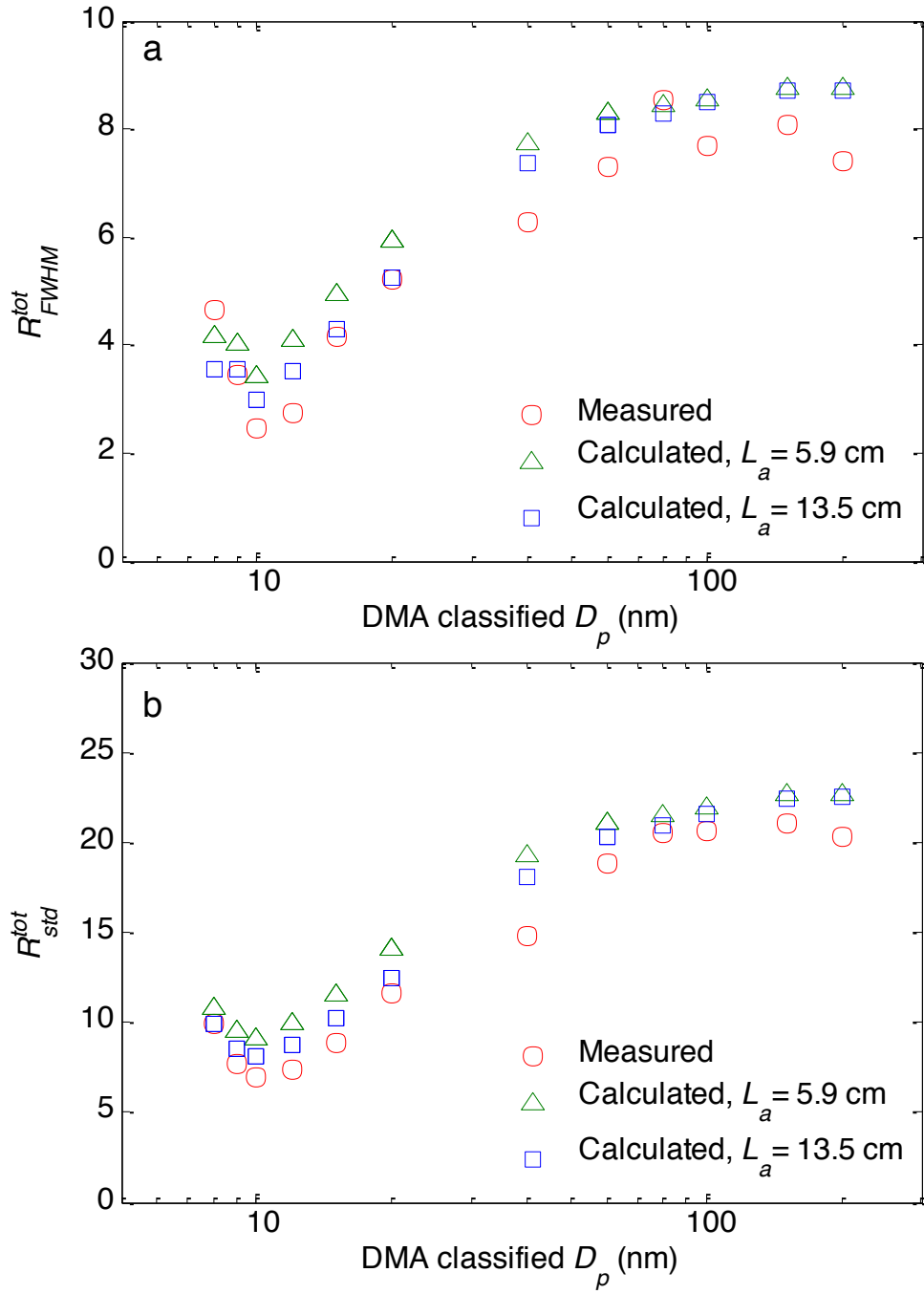
Figure 9. Same as Figure 7, except for particles with x_f between $0.4a$ and $0.5a$.

305   The measured R_{FWHM}^{tot} and R_{std}^{tot} agree with the calculated values well when x_f is limited to a narrow range (e.g., $0.4a \leq x_f \leq 0.5a$, Fig. 9). This confirms that the lower than expected resolutions for particles detected over the entire viewing windows is due to the "shift" of the measured $\frac{dN}{dZ_p^*}$ with x_f. This "shift" is likely due to the non-ideality of the electric field, including the edge effects near the end of the electrode, which is not represented by the 2-D

310   electric field used to simulate particle trajectories. In addition, the flow field may not become fully developed near the aerosol inlet. While the non-ideality of the electric field is likely the main cause, potential flow disturbances near the aerosol inlet entrance may also contribute to the reduced mobility resolutions. The decrease of DMA resolution has been partially attributed to flow disturbance in the aerosol entrance slit (Zhang & Flagan, 1996). Similar flow disturbance

315   near the FIMS aerosol inlet may similarly contribute to the lower total resolution measured, although this impact is likely to be minor given the quite good agreement between measured and calculated total resolutions for particles with diameter less than 20 nm or greater than 200 nm (Fig. 7). As the total resolution is controlled by the combination of DMA and FIMS transfer functions, we cannot exclude the possibility that the lower measured R_{FWHM}^{tot} and R_{std}^{tot} values may

320   be partially due to reduced DMA mobility resolutions as shown in some of the earlier studies (e.g., Jiang et al., 2011; Zhang & Flagan, 1996). The improvement of FIMS resolution, including simulation of particle trajectories using 3-D electric and flow fields inside the FIMS, will be a topic of future study.

        Based on Eq. (5), the standard deviation of Z_p^* for FIMS measured distribution $\frac{dN}{dZ_p^*}$ can

325   be estimated as $\sigma_{Z_p^*}^2 = \sigma_{Z_p^*,DMA}^2 + \sigma_{Z_p^*,FIMS}^2$, where $\sigma_{Z_p^*,DMA}$ and $\sigma_{Z_p^*,FIMS}$ are the standard deviations for the DMA and FIMS transfer functions, respectively. Therefore R_{std} of FIMS can be derived from the measured R_{std}^{tot} and the calculated R_{std} of DMA by:

$$\left(\frac{1}{R_{std,FIMS}} \right)^2 = \left(\frac{1}{R_{std}^{tot}} \right)^2 - \left(\frac{1}{R_{std,DMA}} \right)^2 \tag{8}$$
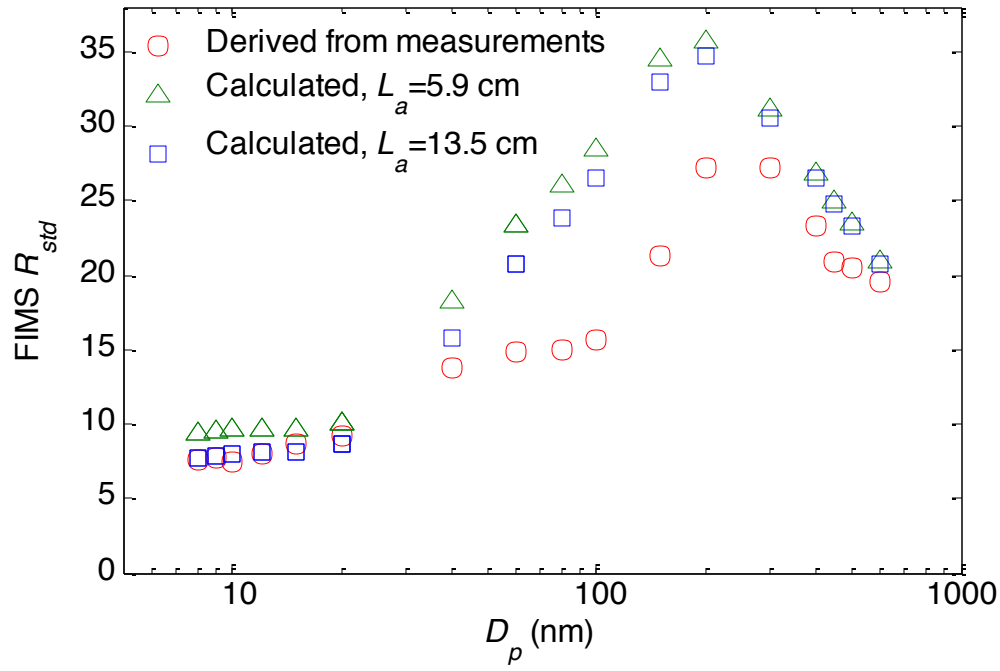
Figure 10. FIMS R_{std} derived from measured R_{std}^{tot} (red circle) and those calculated based on simulated particle trajectories assuming L_a of 5.9 cm (green triangle) and 13.5 cm (blue square), respectively, as function of particle diameter.

The FIMS R_{std} derived from measured R_{std}^{tot} using Eq. (8) generally agree with the calculated R_{std} based on simulated particle trajectories for particles with diameters less than 20 nm or larger than 300 nm (Fig. 10). The agreement for particles with diameters less than 20 nm indicates that the FIMS transfer function and resolution can be well represented by the calculations in this size range, where the FIMS resolution is the lowest due to particle Brownian diffusion. The FIMS mobility resolution is sufficient for measurements of typical aerosols, especially atmospheric aerosols as their size distributions are often much boarder than the width of FIMS transfer function. As the low resolution for particles smaller than 20 nm is mainly due to particle Brownian diffusion, the resolution for small particles could be increased by operating with a higher sheath flow rate, same as in SMPS, although this will lead to a reduced upper size limit. In addition, the FIMS resolution for particles with diameters between 20 and 200 nm could be improved by using only particles detected within a narrower range of x_f as shown in Fig. 9.

4 Conclusions

A Fast Integrated Mobility Spectrometer (FIMS) employing a spatially varying electric field has been developed for rapid measurement of particle size distribution from 8 to 600 nm in diameter. The performance of the FIMS is characterized using monodisperse, DMA classified aerosols in the diameter range of 8 to 600 nm. Particle sizes measured by the FIMS agree well with the DMA centroid diameter determined from DMA flow rates and classifying voltage, suggesting a good sizing accuracy of the FIMS. The counting efficiency of the FIMS is essentially 100% for particles with diameters of 8 nm or larger. The transfer function and mobility resolution of the FIMS are examined. The calculated transfer function of the FIMS reproduces the FIMS responses (i.e., Z_p^* distribution $\frac{dN}{dZ_p^*}$) to DMA classified aerosols well for particles smaller than 20 or larger than 200 nm, indicating that the FIMS transfer function and resolution can be well represented by the calculated quantities for this size range. For DMA classified particles between 20 and 200 nm, the measured Z_p^* distribution is broader than that calculated from FIMS transfer functions. This broader distribution (i.e., lower total resolution) is mainly due to the shift of measured distribution $\frac{dN}{dZ_p^*}$ in Z_p^* space with the variation of detected particle x_f position within the viewing window. The shift is likely a result of non-ideality of the electric field, including edge effects near the end of the electrode, which is not represented by the 2-D electric field used to simulate particle trajectories. Other factors, such as developing flow field inside the separator and degraded mobility resolution of the DMAs, could also contribute to the observed discrepancy. The FIMS resolution is expected to be sufficient for measurements of typical aerosols, especially atmospheric aerosols as their size distributions are often much boarder than the width of FIMS transfer function. The improvement of FIMS resolution, including simulation of particle trajectories using 3-D electric and flow fields inside the FIMS, will be a topic of future study.

References

Jiang, J. K., Attoui, M., Heim, M., Brunelli, N. A., McMurry, P. H., Kasper, G., . . . Mouret, G. (2011). Transfer Functions and Penetrations of Five Differential Mobility Analyzers for Sub-2 nm Particle Classification. *Aerosol Science and Technology, 45*(4), 480-492. doi: 10.1080/02786826.2010.546819

Kulkarni, P., & Wang, J. (2006a). New fast integrated mobility spectrometer for real-time measurement of aerosol size distribution - I: Concept and theory. *J. Aerosol Sci., 37*(10), 1303-1325.

Kulkarni, P., & Wang, J. (2006b). New fast integrated mobility spectrometer for real-time measurement of aerosol size distribution: II. Design, calibration, and performance characterization. *Journal of Aerosol Science, 37*(10), 1326-1339.

Olfert, J. S., Kulkarni, P., & Wang, J. (2008). Measuring aerosol size distributions with the fast integrated mobility spectrometer. *Journal of Aerosol Science, 39*(11), 940-956.

Olfert, J. S., & Wang, J. (2009). Dynamic Characteristics of a Fast-Response Aerosol Size Spectrometer. *Aerosol Science And Technology, 43*(2), 97-111.

Stolzenburg, M. (1988). *An ultrafine aerosol size distribution measuring system.* Ph.D., University of Minnesota, St. Paul.

Wang, J. (2009). A fast integrated mobility spectrometer with wide dynamic size range: Theoretical analysis and numerical simulation. *J. Aerosol Sci., 40*(10), 890-906.

Wang, S. C., & Flagan, R. C. (1990). Scanning Electrical Mobility Spectrometer. *Aerosol Science and Technology, 13*, 230-240.

Zhang, S.-H., & Flagan, R. C. (1996). Resolution of the Radial Differential Mobility Analyzer for Ultrafine Particles. *J. Aerosol Sci., 27*(8), 1179-1200.